JBC RESEARCH ARTICLE

The SARS-CoV-2 Nsp3 macrodomain reverses PARP9/DTX3L-dependent ADP-ribosylation induced by interferon signaling

Received for publication, May 4, 2021, and in revised form, July 16, 2021 Published, Papers in Press, August 4, 2021,
https://doi.org/10.1016/j.jbc.2021.101041

Lilian Cristina Russo[1], Rebeka Tomasin[1], Isaac Araújo Matos[1], Antonio Carlos Manucci[1], Sven T. Sowa[2], Katie Dale[3], Keith W. Caldecott[3], Lari Lehtiö[2], Deborah Schechtman[1], Flavia C. Meotti[1], Alexandre Bruni-Cardoso[1], and Nicolas Carlos Hoch[1,*]

From the [1]Department of Biochemistry, Institute of Chemistry, University of São Paulo, São Paulo, Brazil; [2]Faculty of Biochemistry and Molecular Medicine & Biocenter Oulu, University of Oulu, Oulu, Finland; [3]Genome Damage and Stability Centre, School of Life Sciences, University of Sussex, Falmer, Brighton, United Kingdom

Edited by Craig Cameron

SARS-CoV-2 nonstructural protein 3 (Nsp3) contains a macrodomain that is essential for coronavirus pathogenesis and is thus an attractive target for drug development. This macrodomain is thought to counteract the host interferon (IFN) response, an important antiviral signalling cascade, *via* the reversal of protein ADP-ribosylation, a posttranslational modification catalyzed by host poly(ADP-ribose) polymerases (PARPs). However, the main cellular targets of the coronavirus macrodomain that mediate this effect are currently unknown. Here, we use a robust immunofluorescence-based assay to show that activation of the IFN response induces ADP-ribosylation of host proteins and that ectopic expression of the SARS-CoV-2 Nsp3 macrodomain reverses this modification in human cells. We further demonstrate that this assay can be used to screen for on-target and cell-active macrodomain inhibitors. This IFN-induced ADP-ribosylation is dependent on PARP9 and its binding partner DTX3L, but surprisingly the expression of the Nsp3 macrodomain or the deletion of either PARP9 or DTX3L does not impair IFN signaling or the induction of IFN-responsive genes. Our results suggest that PARP9/DTX3L-dependent ADP-ribosylation is a downstream effector of the host IFN response and that the cellular function of the SARS-CoV-2 Nsp3 macrodomain is to hydrolyze this end product of IFN signaling, rather than to suppress the IFN response itself.

The SARS-CoV-2 pandemic has highlighted the need for an improved understanding of coronavirus pathogenesis for the development of novel antiviral strategies. The interferon (IFN) response is a central component of innate immunity and essentially precludes viral infection, as long as it is properly activated (1, 2). Therefore, successful replication of a virus within host cells requires active suppression or evasion of the host IFN response, which is often mediated by multiple viral proteins acting *via* separate mechanisms (3).

Type I IFN signaling is initiated upon recognition of viral nucleic acids in the cytoplasm, leading to the production and secretion of type I IFNs, such as IFNα and IFNβ, by virus-infected cells, whereas type II IFN, or IFNγ, is secreted by immune cells (1, 4). Binding of these cytokines to transmembrane IFN receptors induces activation of JAK kinases such as TYK2, JAK1, and JAK2, leading to phosphorylation and nuclear translocation of transcription factors of the STAT family, mainly STAT1, and subsequent induction of several hundred interferon-stimulated genes (ISGs) (1, 2). Among these ISGs are several members of the poly(ADP-ribose) polymerase (PARP) family, which catalyze the posttranslational modification of proteins with ADP-ribose units using NAD^+ as a substrate (5).

ADP-ribosylation has recently emerged as a critical regulator of the IFN response, modulating central steps of this signalling cascade, both upstream of Type I IFN production and downstream of Type I or Type II IFN receptor binding (6, 7). Several IFN-regulated PARPs are also antiviral effectors, either by modifying host proteins involved in protein translation, stress granule formation and intracellular protein trafficking, or *via* modification and inhibition of viral proteins directly (6). Interestingly, some of these IFN-responsive PARPs, including PARP9, are rapidly evolving in the primate lineage, suggesting that they are engaged in an "arms race" with viral pathogens (8).

To counteract antiviral ADP-ribosylation by host PARPs, SARS-CoV-2 and other coronaviruses encode a macrodomain within nonstructural protein 3 (Nsp3) that hydrolyzes ADP-ribose modifications (7, 9–11). Importantly, inactivating the mutations within this domain leads to reduced viral replication and increased activation of the host IFN response (12–14), strongly indicating that pharmacological inhibition of the Nsp3 macrodomain may be of substantial therapeutic value (9, 15–17).

Here, we show that activation of Type I or Type II IFN signaling induces ADP-ribosylation of host proteins that can be reversed by ectopic expression of the SARS-CoV-2 Nsp3 macrodomain in human cells. This ADP-ribosylation is

* For correspondence: Nicolas Carlos Hoch, nicolas@iq.usp.br.
Present address for Katie Dale: Department of Oncology, UCL Cancer Institute, University College London, London, United Kingdom.

dependent on the IFN-responsive PARP9/DTX3L heterodimer, but does not seem to modulate IFN signaling itself, since Nsp3 macrodomain expression or PARP9/DTX3L knockout had no effect on STAT1 phosphorylation or the induction of ISGs. We propose that PARP9/DTX3L-dependent ADP-ribosylation of host proteins, which can be reversed by the SARS-CoV-2 Nsp3 macrodomain, is a downstream effector of the IFN response.

Results

To study the functions of the SARS-CoV-2 Nsp3 macrodomain, we first engineered a sensitive assay to detect IFN-induced ADP-ribosylation in human cells. We transfected human A549 lung adenocarcinoma cells with the RNA mimetic poly(I:C), which induces a complete type I IFN cascade (18, 19), or treated these cells with recombinant IFNγ, which induces type II IFN signalling (20, 21). As expected, both treatments led to robust phosphorylation of STAT1 on tyrosine Y701 (Fig. 1*A*), which localized to the cell nucleus (Fig. 1*B*). Using the *Af1521* macrodomain-derived pan-ADP-ribose binding reagent (Millipore, MABE1016) for immunofluorescence staining and a high-content microscopy setup for robust image analysis and signal quantification (Fig. S1 and Experimental procedures section), we observed a pronounced increase in a punctate, cytosolic ADP-ribose signal in response to either poly(I:C) or IFNγ treatment (Fig. 1*C*). Therefore, both type I and type II IFN signaling induce detectable ADP-ribosylation in human cells.

Next, we generated A549 cell lines ectopically expressing FLAG-tagged SARS-CoV-2 Nsp3 macrodomain using lentiviral vectors and confirmed that nearly 100% of the cells express the macrodomain using anti-FLAG immunofluorescence staining (Fig. 2*A*). Strikingly, constitutive macrodomain expression substantially reduced both poly(I:C) or IFNγ-induced ADP-ribosylation compared with empty vector controls (Fig. 2*B*). To confirm these results, we generated cells constitutively expressing a catalytically inactive N40A macrodomain mutant (10, 13) and repeated the experiment with the inclusion of recombinant IFNα and IFNβ. Again, expression of the WT macrodomain substantially reduced ADP-ribosylation induced by all of the treatments tested (Fig. 2*C*). In contrast, expression of the N40A mutant had no appreciable effect on IFN-induced ADP-ribosylation (Fig. 2*C*), indicating that catalytic activity was required for this effect. In these experiments, we observed that the N40A mutant was expressed at lower levels than the WT macrodomain (Fig. S2*A*), which could, in principle, account for the higher persistence of ADP-ribose signal in the population of cells expressing the mutant protein. Therefore, the analysis in Figure 2*C* includes only a subset of cells that express similar levels of WT and N40A macrodomain, based on anti-FLAG immunofluorescence intensity (Fig. S2*B*), which did not alter the original result (Fig. 2*C* and Fig. S2, *C* and *D*). To further strengthen these observations, we generated A549 cell lines with doxycycline-inducible expression of either WT or N40A mutant macrodomain (Fig. S2*E*). As expected, IFNγ-induced ADP-ribosylation was indistinguishable between empty vector controls and either of the uninduced cells (Fig. 2*D*). In agreement with the results above, doxycycline-induced expression of the WT macrodomain reduced ADP-ribosylation, which was once again restored by the N40A mutation (Fig. 2*D*). As before, the cells used in this analysis were gated to ensure similar expression levels between WT and N40A mutant macrodomain, with no effect on the result (Fig. S2, *F* and *G*). Collectively, these data indicate that the Nsp3 macrodomain, when ectopically expressed in human cells, hydrolyzes the ADP-ribosylation of host proteins induced by both type I or type II IFN signaling.

Given the urgent need for antiviral therapies for COVID-19 and the fact that the macrodomain is an attractive therapeutic target (9, 15–17), we attempted to repurpose compounds that already have regulatory approval as potential Nsp3 macrodomain inhibitors. For this, we performed a structure-based virtual screen of a library of 6365 compounds that have been approved for human use by any regulatory agency in the world, against the deposited crystal structures of the SARS-CoV-2 Nsp3 macrodomain bound to ADP-ribose (PDB 6W02) (Fig. 3*A* and methods). Of the final list of 79 compounds of interest, 69 were sourced and tested in biochemical and cellular assays (Table S1). Using thermal shift assays, which measure thermal stabilization of a protein upon ligand binding, we observed that, in contrast to the substantial shift in thermal stability of the Nsp3 macrodomain induced by the ADP-ribose positive control, none of the 69 test compounds showed any evidence of binding to the recombinant macrodomain (Fig. 3*B*). Similar results were obtained in cellular assays, in which none of the compounds substantially restored IFN-induced ADP-ribosylation levels in macrodomain-expressing cells (Fig. 3*C*), and the slight effect of atorvastatin observed in the cellular screen was not confirmed in follow-up experiments (Fig. S3).

Interestingly, we observed that some compounds reduced IFN-induced ADP-ribosylation (Fig. 3*C*) and one of these was tofacitinib, an inhibitor of the JAK kinases that phosphorylate STAT1 in response to IFN receptor activation (22). As expected, tofacitinib treatment completely blocked STAT1-Y701 phosphorylation in response to IFNγ treatment (Fig. 4*A* and Fig. S4*A*), and this resulted in a complete loss of IFN-induced ADP-ribosylation (Fig. 4*B* and Fig. S4*A*). This suggests that ADP-ribosylation is likely to be catalyzed by an IFN-responsive PARP that is transcriptionally induced by STAT1 complexes. This was corroborated by the fact that olaparib, an inhibitor of DNA-damage activated PARPs 1 and 2 that likely also inhibits PARP3, PARP4, and TNKS1/2 (PARP5a/b) at the relatively high concentration used here (23–25) had no effect on IFN-induced ADP-ribosylation or on STAT1 phosphorylation (Fig. 4, *A* and *B* and Fig. S4*A*).

One such IFN-responsive PARP is PARP9, which forms a heterodimer with DTX3L and has been shown to participate in IFN-mediated antiviral responses (26, 27). We had previously generated PARP9 and DTX3L CRISPR knockout cells in an RPE1-hTERT background (Experimental procedures section and Fig. S4, *B* and *C*) and decided to test whether IFN-induced ADP-ribosylation was altered in these cells. As with A549 cells,

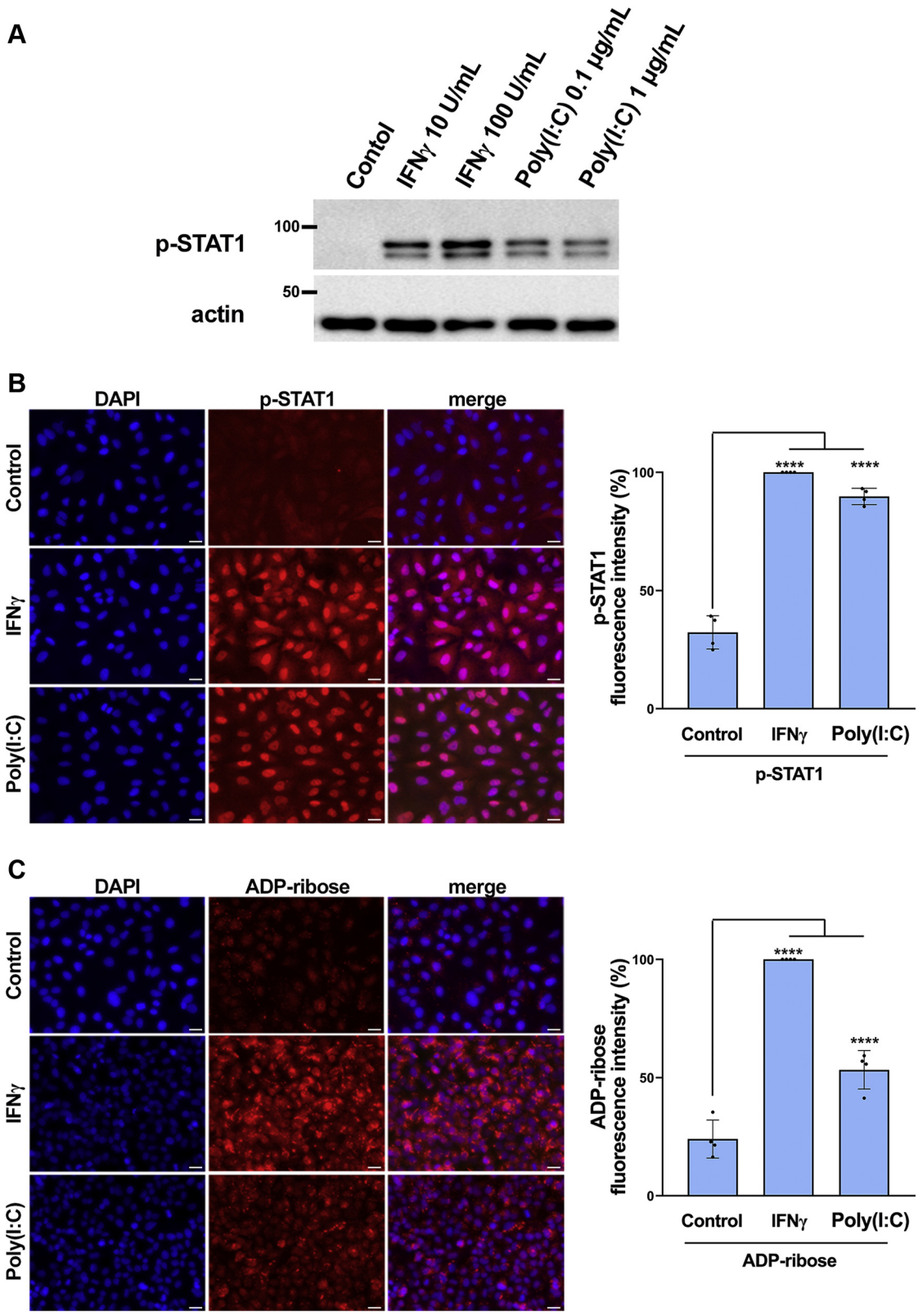

Figure 1. Both type I and type II IFN signaling induce ADP-ribosylation in A549 cells. *A*, immunoblot for STAT1 phospho-Y701 and actin loading control in A549 cells 24 h after treatment with either vehicle control, recombinant interferon gamma (IFNγ), or transfection with poly(I:C), at the doses shown. *B*, *left*, representative images of immunofluorescence staining for STAT1 phospho-Y701 in A549 cells 24 h after treatment with vehicle control, 100 U/ml IFNγ or transfection with 0.1 µg/ml poly(I:C); *right*, quantification of mean p-STAT1 fluorescence per nucleus, averaged for thousands of cells per replicate and normalized to the IFNγ-treated sample. Mean ± SEM (n = 4, from three separate experiments), ****$p < 0.0001$. Scale bars = 20 µm. *C*, *left*, representative images of immunofluorescence staining for ADP-ribose modification (pan-ADP-ribose - Millipore) in A549 cells 24 h after treatment with vehicle control, 100 U/ml IFNγ or transfection with 0.1 µg/ml poly(I:C); *right*, quantification of total ADP-ribose fluorescence in cytosolic dots per cell, averaged for thousands of cells per replicate, and normalized to the IFNγ-treated sample. Mean ± SEM (n = 4, from three separate experiments), ****$p < 0.0001$. Scale bars = 20 µm.

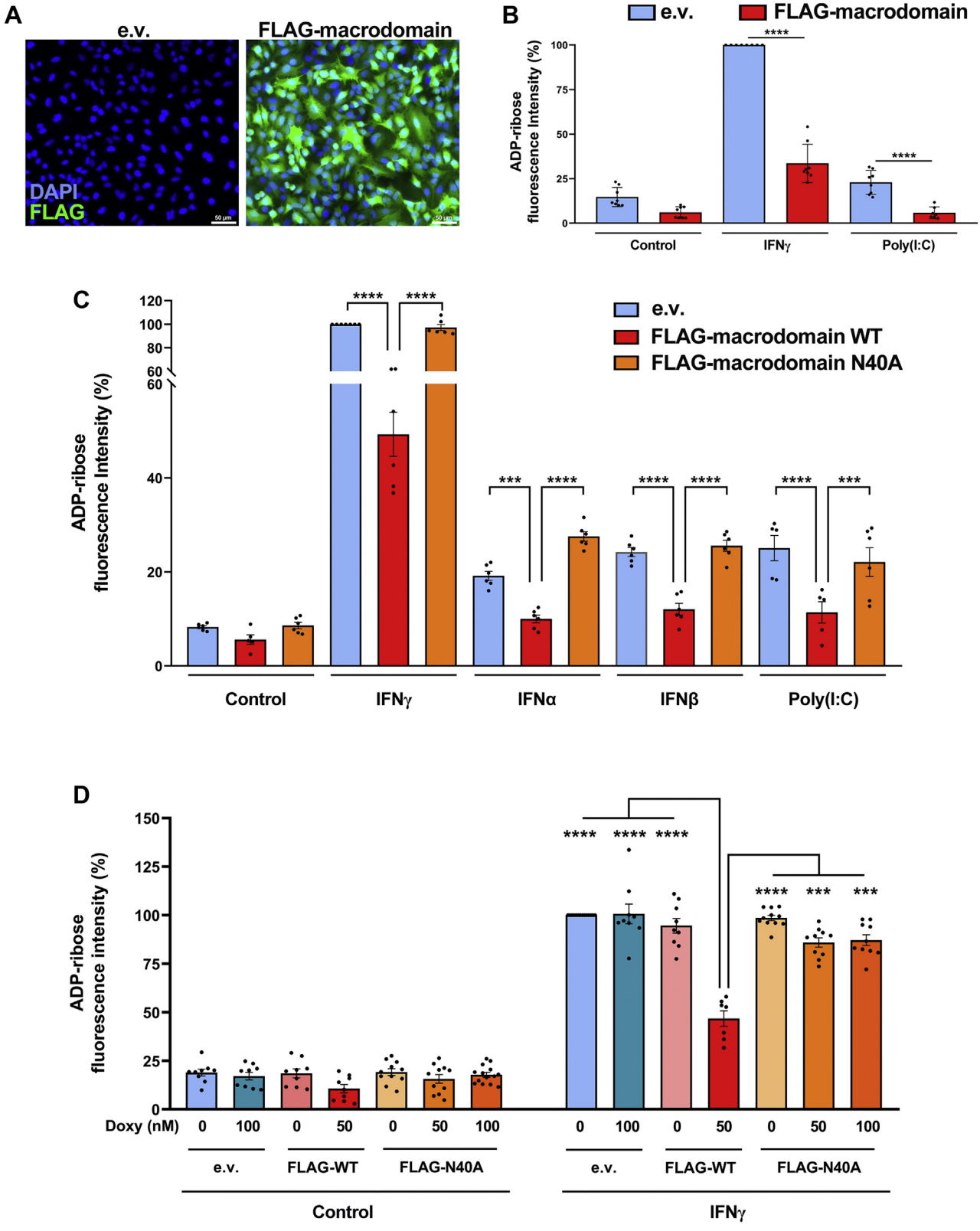

Figure 2. Ectopic expression of the Nsp3 macrodomain reverses IFN-induced ADP-ribosylation. *A*, representative images of anti-FLAG immunofluorescence staining (*green*) and DAPI staining (*blue*) in A549 cells transduced either with an empty vector control (*left*) or with a lentiviral construct constitutively expressing FLAG-tagged SARS-CoV-2 Nsp3 macrodomain (*right*). Scale bars = 20 μm. *B*, quantification of ADP-ribose immunofluorescence signal intensity in A549 cells transduced either with empty vector control (e.v.) or with a lentiviral construct for constitutive expression of FLAG-tagged macrodomain 24 h after treatment with vehicle control, 100 U/ml IFNγ or transfection with 0.1 μg/ml poly(I:C). Mean ± SEM (n = 8, from three separate experiments), $^{****}p < 0.0001$. *C*, quantification of ADP-ribose immunofluorescence signal intensity in A549 cells transduced either with empty vector control (e.v.) or with lentiviral constructs for constitutive expression of either WT macrodomain or catalytically dead N40A mutant, after 24 h treatment with 1000 U/ml IFNα, 1000 U/ml IFNβ, 100 U/ml IFNγ, transfected with 0.1 μg/ml poly(I:C) or vehicle control. For FLAG-macrodomain-expressing samples, cells were gated

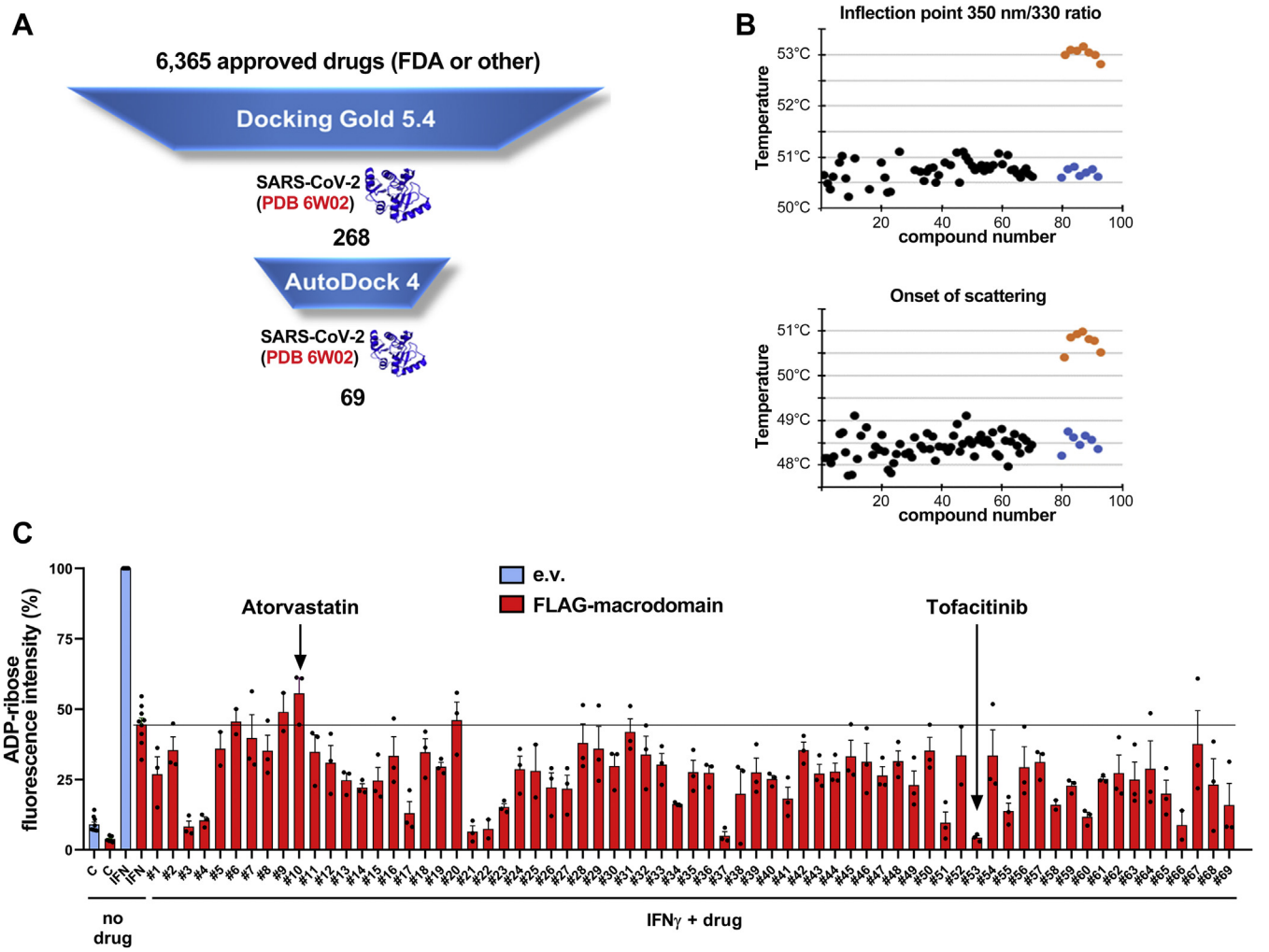

Figure 3. A repurposing screen for macrodomain inhibitors validates the technique for further screening. *A*, virtual screening workflow, starting with 6365 compounds approved for human consumption by any regulatory agency in the world, reaching a final list of 79 compounds taken forward for testing, of which 69 were sourced. *B*, thermal shift assays, by nanoDSF, of the recombinant Nsp3 macrodomain in the absence (*blue*) or presence of 100 μM ADP-ribose (*orange*) or 100 μM of each of the 69 test compounds (*black*). Melting temperatures measured as the inflection point of the 350 nm/330 nm intrinsic fluorescence ratio, indicative of protein unfolding (*top*) and onset of light scattering, indicative of protein aggregation (*bottom*) are shown. *C*, quantification of ADP-ribose immunofluorescence signal intensity in A549 cells transduced either with empty vector control (e.v.) or with a lentiviral construct for constitutive expression of WT macrodomain, 24 h after treatment with vehicle control, 100 U/ml IFNγ or 100 U/ml IFNγ +10 to 50 μM of each of 69 test compounds (Table S1). Mean ± SEM (n = 3). Atorvastatin and tofacitinib (highlighted) are discussed in the main text.

IFNγ treatment induced detectable ADP-ribosylation in RPE1 retinal pigment epithelial cells, confirming that this response is not specific to A549 cells (Fig. 4*C*). Surprisingly, however, PARP9 KO and particularly DTX3L KO cells displayed severely reduced IFNγ-induced ADP-ribosylation compared with controls (Fig. 4*C* and Fig. S4*D*). To determine if this was indirectly caused by an effect of PARP9 or DTX3L knockout on IFN signaling itself, we quantified STAT1-Y701 phosphorylation levels in response to IFNγ treatment in these cells, which revealed that PARP9 KO or DTX3L KO had no appreciable effect on STAT1 phosphorylation (Fig. 4*D*). To ascertain if the reduced ADP-ribosylation in PARP9 KO or DTX3L KO cells may be caused by a defect in IFN signaling downstream of STAT1 phosphorylation, we performed RT-qPCR to assess the transcriptional induction of four IFN-stimulated genes (ISGs)- OAS1, IRF1, ISG15, and Mx1 (28–31) after treatment with either IFNγ or poly(I:C) (Fig. 4*E*). As expected, strong transcriptional induction of these ISGs was observed in RPE1 cells after IFNγ or poly(I:C) treatment, but knockout of PARP9 or DTX3L did not affect the induction of any of these genes under any of the conditions tested (Fig. 4*E*). These data indicate that PARP9 and DTX3L are essential for IFN-induced ADP-ribosylation of host proteins, which occurs downstream of ISG induction.

such that macrodomain expression between WT and N40A mutant was comparable (Fig. S2, *A–C*). Mean ± SEM (n = 6, from three separate experiments), $^{****}p < 0.0001$, $^{***}p < 0.001$. *D*, quantification of ADP-ribose immunofluorescence signal intensity in A549 cells transduced either with empty vector control (e.v.) or with lentiviral constructs for doxycycline-inducible expression of either WT macrodomain or catalytically dead N40A mutant, after 24 h treatment with indicated doses of doxycycline and 100 U/ml IFNγ or vehicle control. For FLAG-macrodomain-expressing samples, cells were gated such that macrodomain expression between WT and N40A mutant was comparable (Fig. S2, *E–G*). Mean ± SEM (n = 7–12, from four separate experiments), $^{***}p < 0.001$ and $^{****}p < 0.0001$.

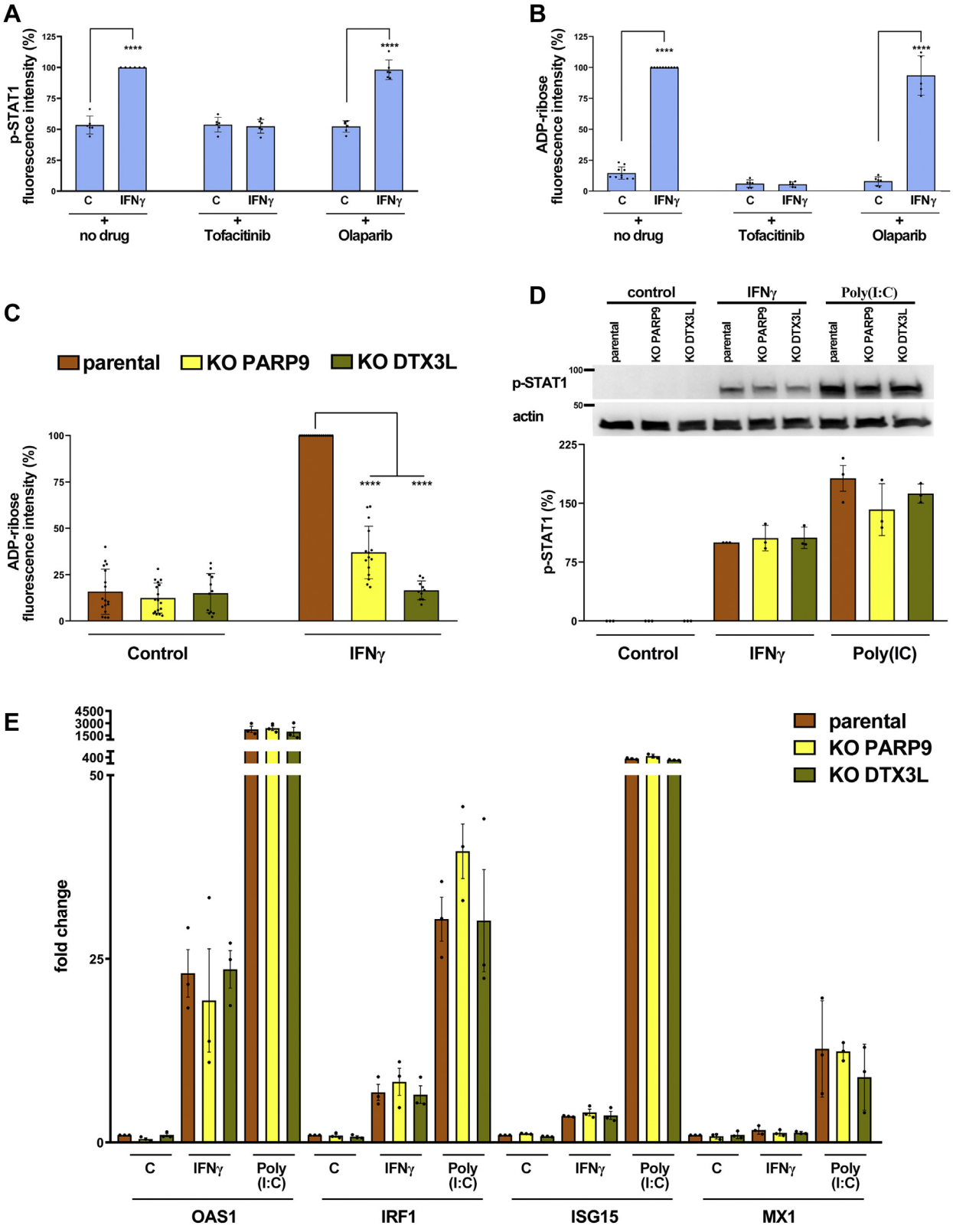

Figure 4. IFN-inducible PARP9 and DTX3L are required for IFN-induced ADP-ribosylation. *A*, quantification of nuclear STAT1 phospho-Y701 immunofluorescence signal intensity in A549 cells 24 h after treatment with vehicle control or 100 U/ml IFNγ, with or without 10 μM tofacitinib or 10 μM olaparib, as indicated. Mean ± SEM (n = 6, from three separate experiments), ****$p < 0.0001$. *B*, quantification of ADP-ribose immunofluorescence signal intensity in A549 cells 24 h after treatment with vehicle control or 100 U/ml IFNγ, with or without 10 μM tofacitinib or 10 μM olaparib, as indicated. Mean ± SEM (n = 6–10, from three separate experiments), ****$p < 0.0001$. *C*, quantification of ADP-ribose immunofluorescence signal intensity in WT, PARP9 or DTX3L KO RPE1-hTERT cells 24 h after treatment with vehicle control or 100 U/ml IFNγ. Mean ± SEM (n = 11–17, from four separate experiments), ****$p < 0.0001$. *D*, representative image (*top*) and quantification (*bottom*) of immunoblot analyses for STAT1 phospho-Y701 and actin loading control in WT, PARP9 KO, or DTX3L KO RPE1-hTERT cells 24 h after treatment with either vehicle control, 100 U/ml IFN γ, or transfection

In light of these results, we decided to determine if Nsp3 macrodomain expression affects host IFN signaling or if its role is also downstream of ISG induction. Consistent with the latter, macrodomain-expressing A549 cells displayed normal levels of STAT1-Y701 phosphorylation by immunofluorescence staining in response to either IFNγ or poly(I:C) treatment (Fig. 5*A*). Expression of the Nsp3 macrodomain also had no effect on the transcriptional induction of four ISGs in response to either IFNγ or poly(I:C) treatment (Fig. 5*B*). In agreement with this, macrodomain expression did not impair STAT1-Y701 phosphorylation or the induction of the IFN-responsive PARP9 or DTX3L proteins after treatment with IFNα, IFNβ, IFNγ, or poly(I:C) (Fig. 5*C* and Fig. S5, *A* and *B*).

To investigate the relative kinetics of IFN-induced JAK/STAT signaling, PARP9/DTX3L protein induction, and ADP-ribosylation, we performed a series of time-course experiments in response to IFNγ, IFNβ, or poly(I:C) (Fig. 5, *D* and *E* and Fig. S5, *C–L*). As expected, STAT1-Y701 phosphorylation peaked at 30 min in response to recombinant IFNs and slowly faded over time, whereas poly(I:C) induced robust STAT1 phosphorylation only at 24 h due to the delayed production of type I IFN by the transfected cells themselves (Fig. 5*E* and Fig. S5, *C*, *F*, *G*, *J* and *K*). Consistent with our previous observations, macrodomain expression did not affect the magnitude or the kinetics of JAK-dependent STAT1 phosphorylation under any of the conditions tested (Fig. 5*E* and Fig. S5, *C*, *F*, *G*, *J* and *K*). Crucially, the kinetics of DTX3L protein induction coincided with the formation of macrodomain-sensitive ADP-ribosylation, both of which started increasing from 4 to 6 h after recombinant IFN treatment, much later than the peak of STAT1 phosphorylation (Fig. 5, *D* and *E* and Fig. S5, *C–L*). Collectively, these data indicate that the Nsp3 macrodomain does not affect the host IFN signaling cascade or the induction of interferon-stimulated genes, but is instead involved in suppressing downstream biological processes triggered by IFN-induced ADP-ribosylation (Fig. 6).

Discussion

Successful viral evasion or suppression of the host interferon response is key for the establishment of a viral infection and is often mediated by several viral factors acting on multiple host targets (3). The coronavirus Nsp3 macrodomain is thought to represent an important mediator of coronavirus pathogenesis by reversing host antiviral ADP-ribosylation and is thus an attractive drug target (7, 9, 15–17). However, little is known about the molecular targets of IFN-responsive PARPs and how reversal of these modifications by the Nsp3 macrodomain may exert its proviral effects.

We have established a cellular immunofluorescence-based assay that can detect the physiological levels of ADP-ribosylation induced by both type I and type II IFN signaling in response to the viral RNA mimetic poly(I:C) or recombinant interferon treatments (Figs. 1 and 2), which is consistent with previous studies showing that IFNγ treatment results in detectable ADP-ribosylation during the process of macrophage activation (32). We demonstrated that ectopically expressed SARS-CoV-2 Nsp3 macrodomain can hydrolyze these modifications in human cells (Fig. 2), which, to our knowledge, had so far only been shown *in vitro* using recombinant coronavirus Nsp3 macrodomains (10, 13).

We have employed this assay in a repurposing screen for Nsp3 macrodomain inhibitors (Fig. 3), which turned out unsuccessful, but highlighted the reasonable throughput of our setup, which allowed two people to perform triplicate screens for 69 compounds in less than a week. Given the shortage of BSL-3 facilities required to test anticoronavirus therapeutics on the SARS-CoV-2 virus directly, and the inherent uncertainty in these tests regarding on-target effects in case of successful reduction in viral loads (33), we believe that a cellular assay such as the one presented here may be a critical intermediate step in the development of Nsp3 macrodomain inhibitors, since a positive result in this assay ensures that candidate compounds are cell-permeable and have on-target effects in human cells.

This microscopy-based assay also allowed us to investigate the origins and functions of the IFN-induced ADP-ribosylation. Interestingly, we observed that Nsp3 macrodomain expression was associated with a slight, but not statistically significant, reduction in ADP-ribosylation even in control cells (Fig. 2, *B–D*). As this effect was also observed upon tofacitinib treatment (Fig. 4*B*), this basal ADP-ribosylation signal may stem from low-level endogenous IFN signaling in A549 cells. Crucially, the signal we detected is predominantly cytosolic and has a punctate pattern (Fig. 1*C*) but, despite extensive efforts, we have so far been unsuccessful in colocalizing this signal with known cytosolic structures and organelles (LCR and NH, unpublished observations). Naturally, it will be critical to identify not only this structure but also the actual protein targets of the Nsp3 macrodomain-sensitive ADP-ribosylation induced by the IFN response, in order to elucidate the putative antiviral function of this modification.

Given that inhibition of DNA damage-responsive PARPs with olaparib had no effect on IFN-induced ADP-ribosylation, but inhibition of JAK kinases completely prevented its formation (Fig. 4, *A* and *B*), our data indicate that the ADP-ribosylation detected here is catalyzed by a PARP whose expression is induced by IFN signaling. Importantly, we identified that the PARP9/DTX3L heterodimer, whose expression is IFN-stimulated (Fig. 5), is absolutely necessary for this ADP-ribosylation, as the signal was lost upon knockout of either of these genes (Fig. 4). Whether PARP9 or DTX3L is individually required for this activity is difficult to determine, as KO of either gene severely affected the stability of the binding partner (Fig. S4*C*), in agreement with previous studies

with 0.1 μg/ml poly(I:C). Mean ± SEM (n = 3). *E*, relative levels of mRNA for OAS1, IRF1, ISG15, and Mx1 genes determined by RT-qPCR in WT, PARP9 KO, or DTX3L KO RPE1-hTERT cells 24 h after treatment with either vehicle control, 100 U/ml IFNγ, or transfection with 0.1 μg/ml poly(I:C), normalized to respective vehicle-treated WT cells. Mean ± SEM (n = 3).

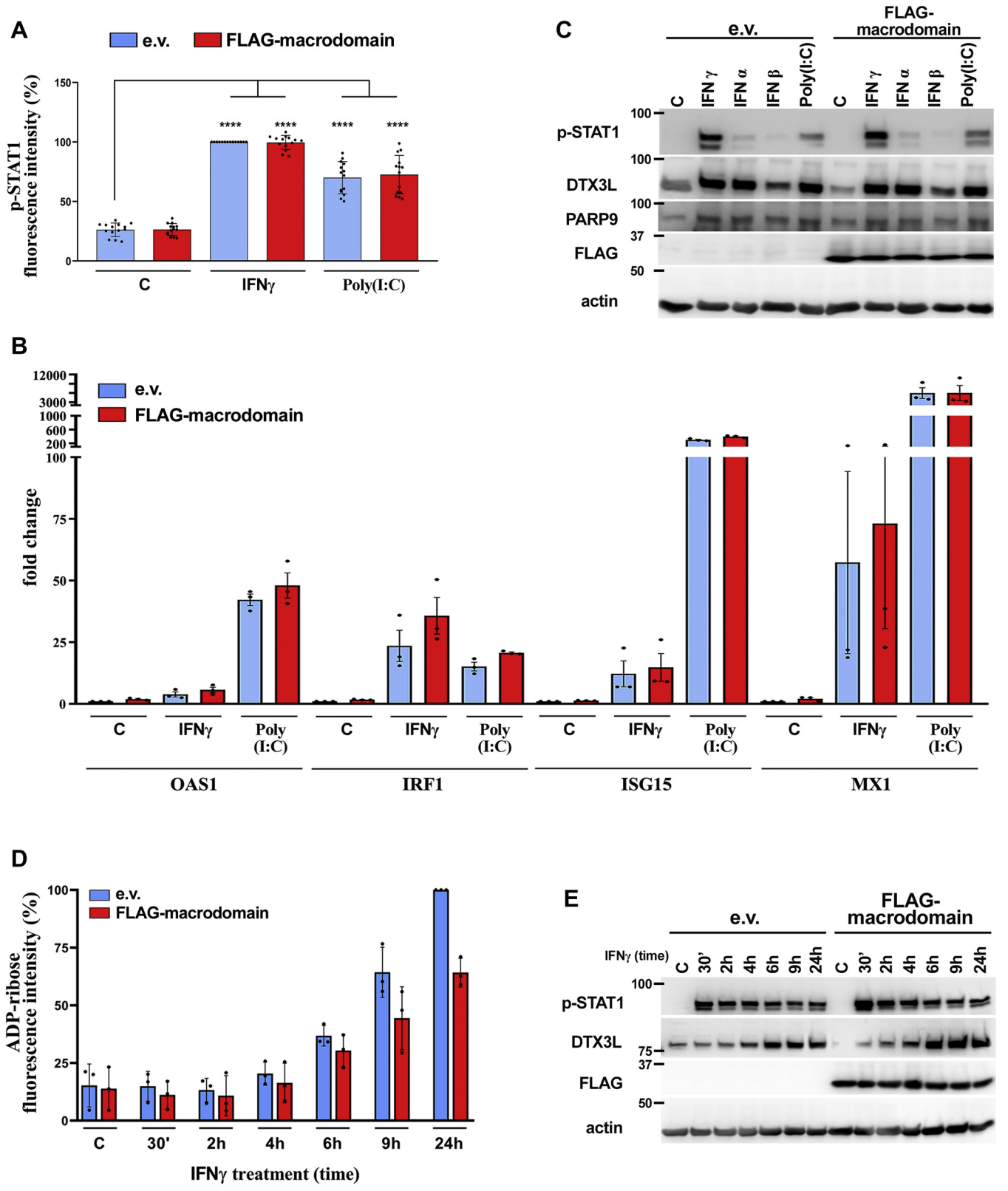

Figure 5. Nsp3 macrodomain expression has no effect on IFN signaling. *A*, quantification of nuclear STAT1 phospho-Y701 immunofluorescence signal intensity in A549 cells transduced either with empty vector control (e.v.) or with a lentiviral construct for constitutive expression of FLAG-tagged macrodomain, 24 h after treatment with vehicle control, 100 U/ml IFNγ, or transfection with 0.1 μg/ml poly(I:C). Mean ± SEM (n = 14, from three separate experiments), ****$p < 0.0001$. *B*, relative levels of mRNA for OAS1, IRF1, ISG15, and Mx1 genes determined by RT-qPCR in A549 cells transduced either with empty vector control (e.v.) or with a lentiviral construct for constitutive expression of FLAG-tagged macrodomain, 24 h after treatment with vehicle control, 100 U/ml IFNγ, or transfection with 0.1 μg/ml poly(I:C), normalized to respective vehicle-treated empty vector control cells. Mean ± SEM (n = 3). *C*, representative image of immunoblot analyses for STAT1 phospho-Y701, DTX3L, PARP9, FLAG, and actin loading control in A549 cells transduced either with empty vector control (e.v.) or with a lentiviral construct for constitutive expression of FLAG-tagged macrodomain, 24 h after treatment with vehicle control,

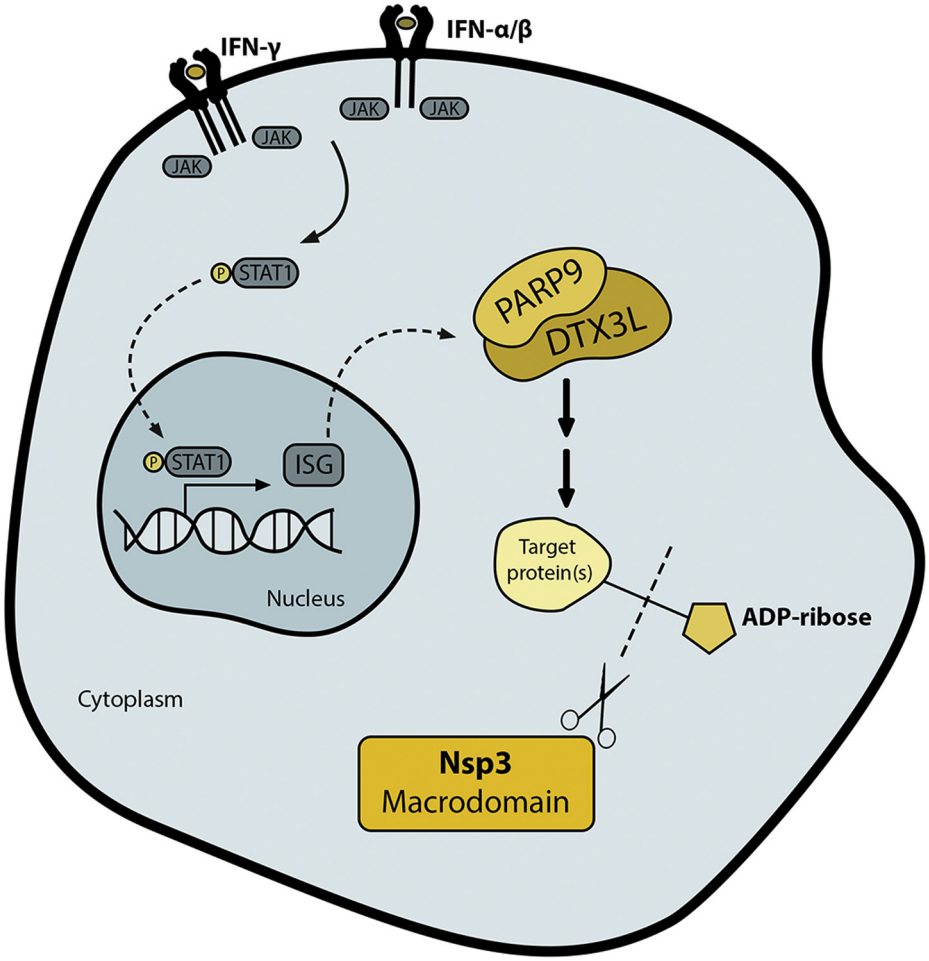

Figure 6. The macrodomain reverses PARP9/DTX3L-dependent ADP-ribosylation induced by IFN signaling. Schematic representation of the proposed model. IFN signaling promotes STAT1 phosphorylation by JAK kinases and induces the expression of interferon-stimulated genes (ISGs), including PARP9 and DTX3L. This complex is required for downstream ADP-ribosylation of target proteins, which is counteracted by the viral Nsp3 macrodomain. Neither PARP9/DTX3L nor the Nsp3 macrodomain affects the IFN signaling cascade itself.

showing codependence of these proteins (26, 27). Interestingly, PARP9 and DTX3L expression is also induced in cells infected with SARS-CoV-2, as long as viral load is high enough to induce an IFN response (34). In agreement with our results, PARP9/DTX3L induction under these conditions is completely prevented by treatment with a JAK kinase inhibitor (34). While it is tempting to speculate that PARP9/DTX3L directly catalyze the formation of the IFN-induced ADP-ribose signal we detected, we cannot rule out a role of these proteins in a putative signaling cascade that culminates in ADP-ribosylation by another PARP.

We propose that the PARP9/DTX3L heterodimer promotes this ADP-ribosylation as a downstream effector of the IFN response, as we did not observe an effect of PARP9/DTX3L deletion on STAT1 phosphorylation or ISG induction (Fig. 4). These data are surprising, considering previous reports showing that PARP9 and DTX3L overexpression increases ISG induction in response to IFN signaling in human fibrosarcoma cells (27) and that PARP9 silencing reduces IFNγ-induced STAT1 phosphorylation and ISG induction in macrophages (35). While further studies are clearly required to clarify the role of PARP9 and DTX3L in the IFN response, we speculate that differences in genetic manipulation of PARP9/DTX3L levels (overexpression, RNA interference, or CRISPR/Cas9 KO) or cell types (fibrosarcoma, macrophage, or retinal pigment epithelia) could account for these differences.

In agreement with our model for an effector function of this PARP9/DTX3L-dependent ADP-ribosylation, the ectopic expression of the Nsp3 macrodomain also had no effect on STAT1 phosphorylation or ISG induction (Fig. 5), despite reversing PARP9/DTX3L-mediated ADP-ribosylation (Fig. 2). This was again surprising, since macrodomain

1000 U/ml IFNα, 1000 U/ml IFNβ, 100 U/ml IFNγ, or transfected with 0.1 μg/ml poly(I:C). Same experiment as Fig. S2*A*, including parts of the same FLAG panel, which came from the same membrane as phospho-STAT1. Actin loading control from same membrane as PARP9. *D*, quantification of ADP-ribose immunofluorescence signal intensity in A549 cells transduced with empty vector control (e.v) or with a lentiviral construct for constitutive expression of FLAG-tagged macrodomain, at indicated timepoints after treatment with 100 U/ml IFNγ. Mean ± SEM (n = 3). *E*, representative image of immunoblot analyses for STAT1 phospho-Y701, DTX3L, FLAG, and actin loading control in A549 cells transduced either with empty vector control (e.v.) or with a lentiviral construct for constitutive expression of FLAG-tagged macrodomain, at indicated timepoints after treatment with 100 U/ml IFNγ.

mutation in a mouse coronavirus model (mouse hepatitis virus- MHV) was previously shown to cause an increase in IFN production by virus-infected murine macrophages (14). In this MHV model, the macrodomain was proposed to mainly counteract PARP14 activity (14), which is thought to act upstream of the production of type I IFN by virus-infected cells (36). These results are not necessarily conflicting, as our methodology may not detect the full complement of IFN-induced ADP-ribosylation or the MHV macrodomain may hydrolyze different PARP targets that play a more prominent role in the mouse IFN response relative to humans (37). Alternatively, macrodomain mutation in the context of a full-length Nsp3 protein may have secondary effects on the activity of other domains, such as the papain-like protease known to suppress IFN signaling (38, 39).

In conclusion, we show here that the SARS-CoV-2 Nsp3 macrodomain hydrolyzes PARP9/DTX3L-dependent ADP-ribosylation induced by IFN signaling and uncover a role for this modification as a putative effector, rather than modulator, of the IFN response (Fig. 6). As part of this study, we developed a cellular assay with the potential to substantially impact drug discovery efforts currently underway to target the Nsp3 macrodomain as a novel anticoronavirus therapy.

Experimental procedures

Cell culture and treatment conditions

A549 lung adenocarcinoma cells were grown in DMEM/high glucose media (Thermo) and RPE1-hTERT retinal pigment epithelia cells were grown in DMEM/F-12, both supplemented with 10% Fetal Bovine Serum (Thermo). HEK293 FT cells were grown in DMEM/high glucose supplemented with 10% FBS (Thermo), 50 mg/ml gentamycin (Sigma), 1 mM sodium pyruvate (Thermo), nonessential amino acids (Thermo), and 2 mM L-glutamine (Thermo). All cell lines were maintained at 37 °C in a humidified atmosphere containing 5% CO_2. Recombinant interferons α, β, and γ (Sigma SRP4594, I9032, and SRP3058) were added directly to the media at the indicated doses and poly(I:C) (Sigma) was transfected using PEI and the cells collected 24 h later. Tofacitinib (Selleckchem), olaparib (Selleckchem), or atorvastatin (Sigma) was added at the indicated doses at the same time as the induction of IFN signaling.

Lentiviral construct generation and viral transduction

SARS-CoV2-Nsp3 macrodomain (UniProt identifier P0DTC1, residues 1023–1157) was amplified from a pET30a-based vector (a kind gift by A.Fehr - Univ. of Kansas) and cloned *via* BamHI and XhoI sites into a pCDNA3.1-based vector previously engineered to contain an N-terminal FLAG-FLAG-Strep-Strep tag. This ORF was then subcloned into a pCDH-puro lentiviral vector (System Biosciences) *via* NheI and XhoI sites or amplified and cloned *via* EcoRI and AgeI sites into the pLVX-TetOne-puro lentiviral vector (System Biosciences). The N40A mutation was generated by standard site-directed mutagenesis and all vectors were confirmed by Sanger sequencing of the inserts. These vectors were cotransfected with psPAX2 and pMD2.G packaging vectors (Systems Biosciences) into HEK-293FT cells using standard PEI transfection, the supernatant collected 48 h and 72 h after transfection, filtered through 0.45 μm filters, and used to transduce A549 cells in the presence of 8 μg/ml polybrene (Sigma). After 48 h, 5 μg/ml puromycin was added to the media for selection of transduced cells for 7 days.

Virtual screening

The crystal structure of the Nsp3 macrodomain from SARS-CoV-2 cocrystallized with ADP-ribose (Protein Data Bank code 6W02) was used for structure-based studies (40). The protonation states of residues were revised and the variable conformation of the Asp27 residue was adjusted. Hydrogen atoms were added and water molecules and ligands were removed. Molecular docking simulations were performed with Gold 5.4 and AutoDock 4.2.3 softwares. The protein was set as rigid and the ligands as flexible. For the docking studies using Gold 5.4, the radius of simulation was set to 6 Å (considering the large size of ADP-ribose). CHEMPLP score function was selected and the efficiency parameter set to very flexible, while other parameters were left at default values. For the docking with AutoDock, nonpolar hydrogen atoms were merged with respective carbons and Gasteiger charges were added. The number of points of each dimension was 25 × 40 × 50 Å and grid box was centralized in the coordinates 10.649 × 7.101 × 20.841. For each ligand, 100 simulations of molecular docking were performed. For optimization, Lamarckian genetic algorithms were employed and the molecular docking protocols were validated by redocking. For this, cocrystallized ADP-ribose was removed and redocked in PDB 6W02. RMSD distances between experimental and simulated atom ligands were calculated by VMD (41). For virtual screening, the subset of 6365 drugs approved in the world available in Zinc15 (http://zinc15.docking.org/) was selected as target library.

Cloning of expression vectors and purification of recombinant protein

The SARS-CoV-2 Nsp3 macrodomain (Uniprot identifier P0DTC1, residues 1024–1192) was cloned into pNH-TrxT vector (Addgene plasmid #26106) using SLIC restriction-free cloning method (42). Briefly, the pNH-TrxT plasmid was linearized and 100 ng of linearized plasmid was mixed in a 1:4 M ratio with SARS-CoV-2 Nsp3 macrodomain (gBlock gene fragment, Integrated DNA Technologies) and incubated with T4 DNA polymerase for 2.5 min at room temperature and for 10 min on ice. The mixture was used to transform NEB5α competent *E. coli* cells (New England BioLabs) according to manufacturer's instructions. Colonies were grown on LB agar containing 5% sucrose using the SacB-based negative selection marker (43). The construct was verified by sequencing of the insert regions and was then used to transform *E. coli* BL21(DE3) cells. In total, 500 ml Terrific Broth (TB) autoinduction media including trace elements

(Formedium, Hunstanton, Norfolk, England), supplemented with 8 g/l glycerol and 50 μg/ml kanamycin, was inoculated with 5 ml of overnight preculture and incubated at 37 °C until an OD600 of 1 was reached. After an overnight incubation at 16 °C, the cells were collected by centrifugation at 4200*g* for 30 min at 4 °C. The pellets were resuspended in lysis buffer (50 mM HEPES pH 7.5, 500 mM NaCl, 10 mM imidazole, 10% glycerol, 0.5 mM TCEP) and stored at −20 °C. For protein purification, the cells were thawed and lysed by sonication. The lysate was centrifuged (16,000*g*, 4 °C, 30 min), filtered and loaded onto a 5 ml HiTrap HP column equilibrated with lysis buffer, and charged with Ni^{2+}. The column was washed with 30 column volumes of lysis buffer and four column volumes of wash buffer (30 mM HEPES pH 7.5, 30 mM imidazole, 500 mM NaCl, 10% glycerol, 0.5 mM TCEP). The protein was eluted using wash buffer containing 300 mM imidazole. Imidazole was removed by dialysis and TEV-protease was added (1:30 M ratio, 16 h, 4 °C) to cleave the His_6-TrxT-tag followed by a reverse IMAC step to remove impurities. Size-exclusion chromatography was carried out on a HiLoad 16/600 Superdex 75 pg 120 ml column in 30 mM HEPES pH 7.5, 300 mM NaCl, 10% glycerol and 0.5 mM TCEP. Pure fractions were pooled and stored at −70 °C.

Thermal shift assay

The purified SARS-CoV-2 Nsp3 macrodomain was diluted to 0.3 mg/ml in assay buffer (25 mM HEPES pH 7.5, 100 mM NaCl) and mixed with 100 μM of the compounds. The sample containing Flubendazole was measured at 20 μM compound concentration due to limited solubility. Samples in the presence or absence of 100 μM ADP-ribose were used as controls. All samples and controls contained a final concentration of 1%(v/v) DMSO. Samples were loaded to glass capillaries and analysis was performed in Prometheus NT.48 (NanoTemper). Data points were recorded from 35 to 65 °C, with the temperature increasing by 1 °C/min. The onset of scattering and melting temperatures based on the change of intrinsic protein fluorescence (ratio 350 nm/330 nm) was calculated in PR.ThermControl software (NanoTemper).

CRISPR/Cas9 knockout generation

PARP9 and DTX3L sgRNA sequences were 5′ GATCTGATGGGATTCAACG (exon 8) and 5′GCAGTTCG CTGTATTCCA (exon 4), respectively. Appropriate oligonucleotides were annealed, phosphorylated, and cloned into BbsI-digested eSpCas9(1.1) vector (Addgene #71814). We subsequently discovered that these gRNAs, which were designed as tru-gRNAs with 17 bp of homology plus a 5′G (44) are incompatible with the eSpCas9(1.1) mutant (45). Therefore, RPE1-hTERT cells were cotransfected with either of these vectors and the hCas9 vector (Addgene #41815) using a Neon Transfection system (Thermo) and transfected cells selected with G418 for 5 days. Individual clones were screened by western blotting and clones with complete absence of PARP9 and DTX3L protein were selected (Fig. S4*B*). Genomic DNA surrounding the edited locus was amplified and analyzed by Sanger sequencing (Fig. S4*C*).

Western blotting

Adherent cells were washed in PBS and lysed directly in preheated Laemmli buffer devoid of bromophenol blue and beta-mercaptoethanol. Lysates were transferred to tubes, boiled for 15 min, and the protein concentration was determined using BCA protein quantification kit (Pierce). After normalization of protein concentrations and addition of bromophenol blue and beta-mercaptoethanol, samples were boiled again for 10 min, and 15 to 50 μg of protein was loaded per sample in standard SDS-PAGE gels. Proteins were transferred to nitrocellulose membranes (Bio-Rad), visualized with Ponceau Red (Sigma), and the membranes were cut horizontally such that different portions of the same membrane could be incubated with the appropriate antibodies. Membranes were blocked with 5% BSA for 30 min and incubated with primary antibody overnight at 4 °C. After extensive washing in TBST buffer, 1 h incubation in appropriate HRP-conjugated secondary antibodies (Sigma), and another round of washing, membranes were incubated with ECL Prime (Amersham), and the signal was detected using a Chemidoc MP Imaging System (Bio-Rad). Signals were quantified using ImageJ software.

Immunofluorescence staining

Cells were seeded either on 1.5H glass coverslips (Thorlabs) or in microscopy-compatible plastic 96-well plates (Corning), treated as required, washed with PBS, and fixed with 2% (for pSTAT1) or 4% EM-grade PFA (EMS) prepared in PBS, which was subsequently quenched with 0.1 M glycine. After permeabilization in 100% methanol (for pSTAT1) or 0.2% TritonX-100 in PBS, samples were blocked in 1% BSA/5% goat serum in PBS and incubated with primary antibody for 1 h at room temperature (for ADP-ribose) or overnight at 4 °C. Samples were extensively washed in PBS, incubated with appropriate fluorescently labeled secondary antibodies (Thermo), washed again, stained with DAPI (Thermo), and the coverslips were mounted in Vectashield (Vector Labs) or the plates were maintained in 90% glycerol until image acquisition.

Image acquisition and analysis

Fluorescence microscopy images were acquired on a customized TissueFAXS i-Fluo system (TissueGnostics) mounted on a Zeiss AxioObserver 7 microscope (Zeiss), using 20× Plan-Neofluar (NA 0.5) or 40× Plan-Apochromat (NA 0.95) objectives and an ORCA Flash 4.0 v3 camera (Hamamatsu). For most experiments, 6 × 6 adjacent fields of view were acquired per sample using automated autofocus and image acquisition settings. Images were analyzed using StrataQuest software (TissueGnostics). For phospho-STAT1 quantification, individual nuclei were detected in the DAPI channel and the mean intensity of phospho-STAT1 signal per nucleus quantified for thousands of cells per sample. For ADP-ribose quantification, individual nuclei were detected in the DAPI channel

Table 1
Oligonucleotides sequences and their functions

Oligo name	Sequence	Function
F-BamHI-MD	GAAAGAACGGATCCATGATT GAAGTGAATAGTTTTAGTGG	Amplification of Macrodomain sequence from pET30a vector fw (contains BamHI site)
R-MD-XhoI	GTGGTGCTCGAGTTACTTTTCA CTCTTCATTTCC	Amplification of Macrodomain sequence from pET30a vector rev (contains XhoI site)
Fw-EcoRI-FFSS	TATGCGAATTCGCCACCATGGA CTACAAGGACGA	Amplification of FLAG-macrodomain from pCDH vector fw (contains EcoRI site)
Rv-AgeI-MD2	TATGCACCGGTTTACTTTTCACTCTTCATTT	Amplification of FLAG-macrodomain from pCDH vector rev (contains AgeI site)
N40A fw	GTGGTTGTTAATGCAGCTGCAGTTTACCTTAAACAT GGA	Site directed mutagenesis for N40A mutation fw (creates PstI site)
N40A rev	TCCATGTTTAAGGTAAACTGCAGCTGCATTAACAAC CAC	Site directed mutagenesis for N40A mutation rev (creates PstI site)
PARP9 gRNA fw	CACCGATCTGATGGGATTCAACG	Oligonucleotide for cloning of PARP9 gRNA into peSp-Cas9(1.1) fw (with overhangs for cloning)
PARP9 gRNA rev	AAACCGTTGAATCCCATCAGATC	Oligonucleotide for cloning of PARP9 gRNA into peSp-Cas9(1.1) rev (with overhangs for cloning)
DTX3L gRNA fw	CACCGCAGTTCGCTGTATTCCA	Oligonucleotide for cloning of DTX3L gRNA into peSp-Cas9(1.1) fw (with overhangs for cloning)
DTX3L gRNA rev	AAACTGGAATACAGCGAACTGC	Oligonucleotide for cloning of DTX3L gRNA into peSp-Cas9(1.1) rev (with overhangs for cloning)
PARP9 check fw	GTCATTTCAGTCCCCCAGTC	Amplification of edited PARP9 locus for sequencing fw/ sequencing primer
PARP9 check rev	CTTTTGGGTGTGAGCGTGTA	Amplification of edited PARP9 locus for sequencing rev
DTX3L check fw	TGCTTTTGATTTGCTTTATCTACAA	Amplification of edited DTX3L locus for sequencing fw
DTX3L check rev	AGTGGGGTACTCTCGCGTATT	Amplification of edited DTX3L locus for sequencing rev/ sequencing primer
OAS1 fw	TGCGCTCAGCTTCGTACTGA	qPCR forward primer for OAS1 gene
OAS1 rev	GGTGGAGAACTCGCCCTCTT	qPCR reverse primer for OAS1 gene
IRF1 fw	CCAAGAGGAAGTCATGTG	qPCR forward primer for IRF1 gene
IRF1 rev	TAGCCTGGAACTGTGTAG	qPCR reverse primer for IRF1 gene
ISG15 fw	GGGACCTGACGGTGAAGATG	qPCR forward primer for ISG15 gene
ISG15 rev	CGCCGATCTTCTGGGTGAT	qPCR reverse primer for ISG15 gene
MX1 fw	ACATCCAGAGGCAGGAGACAATC	qPCR forward primer for MX1 gene
MX1 rev	TCCACCAGATCAGGCTTCGTCAA	qPCR reverse primer for MX1 gene
RPL19 fw	GATCGATCGCCACATGTATCAC	qPCR forward primer for RPL19 gene (housekeeping)
Rpl19 rev	TTGTCTGCCTTCAGCTTGTG	qPCR reverse primer for RPL19 gene (housekeeping)

and the approximate cell boundaries determined by growing outward from the nuclear area for a fixed distance, until neighboring areas touched each other or until the ADP ribose signal reached background levels. Peaks of ADP-ribose signal intensity within this cellular mask (excluding the nucleus) were detected as "dots" and the total fluorescence signal contained in all dots per cell was quantified for thousands of cells per sample. In both cases, the fluorescence intensities of all cells within a sample were averaged, and this value normalized to the average intensity of the IFNγ-treated control sample for each biological replicate experiment (Fig. S1).

RT-qPCR

Total RNA was extracted from 10^6 cells using an RNAeasy kit (Qiagen), treated with DNAseI (Ambion) and reverse-transcribed using SuperScriptII (Thermo), according to manufacturer's instructions, using both oligodT and random hexamer primers (Thermo). This cDNA was used for qPCR (5 ng/reaction) using Power SYBR green Master mix (Thermo) with three technical replicates per biological replicate, using 200 nM of the primer sets indicated in Table 1, which were chosen from PrimerBank (46). Reactions were performed on an Applied Biosystems 7500 Real-time PCR system, using

Table 2
Antibodies and their respective applications

Antibody	Host species	Supplier (catalogue number)	Application (dilution)
Actin	Mouse	Millipore (MAB1501)	WB (1:5000)
pan-ADP-ribose	Rabbit	Millipore (MABE1016)	IF (1:400) (all experiments)
pan-ADP-ribose	Mouse	A kind gift by M. Hottiger (47)	IF (1:400) (data not shown)
PARP9	Rabbit	Thermo (40-4400)	WB (1:500)
DTX3L	Rabbit	Bethyl (A300-834A)	WB (1:1000)
STAT1 phospho-Y701	Rabbit	Cell Signalling (9167)	IF (1:400) and WB (1:1000)
FLAG	Mouse	Sigma (F1804)	IF (1:400) and WB (1:1000)
Anti-Rabbit-HRP	Donkey	Sigma (SAB3700934-2MG)	WB (1:5000)
Anti-Mouse-HRP	Donkey	Sigma (SAB3701105-2MG)	WB (1:5000)
Anti-Mouse-AF488	Donkey	Thermo (A21202)	IF (1:400)
Anti-Rabbit-AF488	Donkey	Thermo (A21206)	IF (1:400)
Anti-Mouse-AF568	Donkey	Thermo (A10037)	IF (1:400)
Anti-Rabbit-AF568	Donkey	Thermo (A10042)	IF (1:400)
Anti-Mouse-AF647	Donkey	Thermo (A32787)	IF (1:400)
Anti-Rabbit-AF647	Donkey	Thermo (A32795)	IF (1:400)

default settings. RPL19 was used as housekeeping control and standard $2^{-\Delta\Delta Ct}$ analysis performed relative to the untreated control sample.

Statistical analyses

All experiments were repeated on at least three separate occasions, often with multiple parallel replicates processed on the same day, but treated as independently as possible. All graphs and statistical analyses were generated using GraphPad Prism software and display both the distributions of individual datapoints and their mean ± SEM of the normalized values relative to the IFNγ-treated control for each replicate, considered as 100%. Statistical comparisons between samples were performed using ANOVA, with $p < 0.0001$ indicated by ****, $p < 0.001$ indicated by *** and $p < 0.01$ indicated by **.

Primers and antibodies

All oligonucleotides and antibodies used in this study are presented in Tables 1 and 2

Data availability

The datasets generated during the current study are available from the corresponding author on reasonable request.

Supporting information—This article contains supporting information.

Acknowledgments—The authors wish to thank Anthony Fehr (Univ. Kansas) for the macrodomain vector used for cloning and fruitful discussions; Michael Hottiger (Univ. Zurich) for an ADP-ribose-binding reagents; Heli Alanen (Univ. Oulu) for production of the recombinant SARS-CoV-2 macrodomain; Célia Braga (Univ. São Paulo) for technical assistance; Priscilla Doria (Univ. São Paulo) for designing the graphical abstract; and several colleagues from the University of São Paulo and from local pharmaceutical companies who helped source some of the compounds used for screening. The use of the facilities and expertise of the Proteomics and Protein Analysis core facility (a member of Biocenter Finland) and Biocenter Oulu sequencing center are gratefully acknowledged.

Author contributions—L. C. R., R. T., I. A. M., A. C. M., S. T. S., K. D., and N. C. H. investigation; D. S., F. C. M., A. B.-C., K. W. C., L. L., and N. C. H. methodology; D. S., F. C. M., A. B.-C., K. W. C., L. L., and N. C. H. supervision; N. C. H. project administration; N. C. H. writing–original draft.

Funding and additional information—Work in the N. C. H. lab is supported by a COVID19 emergency grant (2020/53017-6) and a Young Investigator Award (2018/18007-5) from FAPESP, L. C. R. is funded by a FAPESP post-doctoral fellowship and held a Dimensions Sciences short-term fellowship, R. T. is funded by a PNPD/CAPES postdoctoral fellowship, A. C. M. and I. A. M. hold PhD scholarships from CNPq, the F. C. M. lab is supported by a FAPESP Young Investigator II Award (2018/14898-2), and work in the A. B.-C. lab is funded by FAPESP grant 2019/26767-2. Work in the L. L. lab was funded by the Jane and Aatos Erkko Foundation and by the Academy of Finland (grant nos. 287063, 294085, and 319299 to L. L.).

Conflict of interest—The authors declare that they have no conflicts of interest with the contents of this article.

Abbreviations—The abbreviations used are: IFN, interferon; ISG, interferon-stimulated gene; Nsp3, nonstructural protein 3; PARP, poly(ADP-ribose) polymerase.

References

1. Ivashkiv, L. B., and Donlin, L. T. (2014) Regulation of type I interferon responses. *Nat. Rev. Immunol.* **14**, 36–49
2. Schoggins, J. W. (2019) Interferon-stimulated genes: What do they all do? *Annu. Rev. Virol.* **6**, 567–584
3. Garcia-Sastre, A. (2017) Ten strategies of interferon evasion by viruses. *Cell Host Microbe* **22**, 176–184
4. Lee, A. J., and Ashkar, A. A. (2018) The dual nature of type I and type II interferons. *Front. Immunol.* **9**, 2061
5. Hoch, N. C., and Polo, L. M. (2019) ADP-ribosylation: From molecular mechanisms to human disease. *Genet. Mol. Biol.* **43**, e20190075
6. Fehr, A. R., Singh, S. A., Kerr, C. M., Mukai, S., Higashi, H., and Aikawa, M. (2020) The impact of PARPs and ADP-ribosylation on inflammation and host-pathogen interactions. *Genes Dev.* **34**, 341–359
7. Hoch, N. C. (2021) Host ADP-ribosylation and the SARS-CoV-2 macrodomain. *Biochem. Soc. Trans.* https://doi.org/10.1042/BST20201212
8. Daugherty, M. D., Young, J. M., Kerns, J. A., and Malik, H. S. (2014) Rapid evolution of PARP genes suggests a broad role for ADP-ribosylation in host-virus conflicts. *PLoS Genet.* **10**, e1004403
9. Alhammad, Y. M. O., and Fehr, A. R. (2020) The viral macrodomain counters host antiviral ADP-ribosylation. *Viruses* **12**, 384
10. Alhammad, Y. M. O., Kashipathy, M. M., Roy, A., Gagne, J. P., McDonald, P., Gao, P., Nonfoux, L., Battaile, K. P., Johnson, D. K., Holmstrom, E. D., Poirier, G. G., Lovell, S., and Fehr, A. R. (2021) The SARS-CoV-2 conserved macrodomain is a mono-ADP-ribosylhydrolase. *J. Virol.* **95**, e01969-20
11. Leung, A. K. L., McPherson, R. L., and Griffin, D. E. (2018) Macrodomain ADP-ribosylhydrolase and the pathogenesis of infectious diseases. *PLoS Pathog.* **14**, e1006864
12. Fehr, A. R., Athmer, J., Channappanavar, R., Phillips, J. M., Meyerholz, D. K., and Perlman, S. (2015) The Nsp3 macrodomain promotes virulence in mice with coronavirus-induced encephalitis. *J. Virol.* **89**, 1523–1536
13. Fehr, A. R., Channappanavar, R., Jankevicius, G., Fett, C., Zhao, J., Athmer, J., Meyerholz, D. K., Ahel, I., and Perlman, S. (2016) The conserved coronavirus macrodomain promotes virulence and suppresses the innate immune response during severe acute respiratory syndrome coronavirus infection. *mBio* **7**, e01721-16
14. Grunewald, M. E., Chen, Y., Kuny, C., Maejima, T., Lease, R., Ferraris, D., Aikawa, M., Sullivan, C. S., Perlman, S., and Fehr, A. R. (2019) The coronavirus macrodomain is required to prevent PARP-mediated inhibition of virus replication and enhancement of IFN expression. *PLoS Pathog.* **15**, e1007756
15. Brosey, C. A., Houl, J. H., Katsonis, P., Balapiti-Modarage, L. P. F., Bommagani, S., Arvai, A., Moiani, D., Bacolla, A., Link, T., Warden, L. S., Lichtarge, O., Jones, D. E., Ahmed, Z., and Tainer, J. A. (2021) Targeting SARS-CoV-2 Nsp3 macrodomain structure with insights from human poly(ADP-ribose) glycohydrolase (PARG) structures with inhibitors. *Prog. Biophys. Mol. Biol.* **163**, 171–186
16. Rack, J. G. M., Zorzini, V., Zhu, Z., Schuller, M., Ahel, D., and Ahel, I. (2020) Viral macrodomains: A structural and evolutionary assessment of the pharmacological potential. *Open Biol.* **10**, 200237
17. Schuller, M., Correy, G. J., Gahbauer, S., Fearon, D., Wu, T., Diaz, R. E., Young, I. D., Carvalho Martins, L., Smith, D. H., Schulze-Gahmen, U., Owens, T. W., Deshpande, I., Merz, G. E., Thwin, A. C., Biel, J. T., *et al.* (2021) Fragment binding to the Nsp3 macrodomain of SARS-CoV-2

identified through crystallographic screening and computational docking. *Sci. Adv.* **7**, eabf8711
18. Field, A. K., Tytell, A. A., Lampson, G. P., and Hilleman, M. R. (1967) Inducers of interferon and host resistance. II. Multistranded synthetic polynucleotide complexes. *Proc. Natl. Acad. Sci. U. S. A.* **58**, 1004–1010
19. Matsumoto, M., and Seya, T. (2008) TLR3: Interferon induction by double-stranded RNA including poly(I:C). *Adv. Drug Deliv. Rev.* **60**, 805–812
20. Kang, S., Brown, H. M., and Hwang, S. (2018) Direct antiviral mechanisms of interferon-gamma. *Immune Netw.* **18**, e33
21. Wheelock, E. F. (1965) Interferon-like virus-inhibitor induced in human leukocytes by phytohemagglutinin. *Science* **149**, 310–311
22. Ghoreschi, K., Jesson, M. I., Li, X., Lee, J. L., Ghosh, S., Alsup, J. W., Warner, J. D., Tanaka, M., Steward-Tharp, S. M., Gadina, M., Thomas, C. J., Minnerly, J. C., Storer, C. E., LaBranche, T. P., Radi, Z. A., *et al.* (2011) Modulation of innate and adaptive immune responses by tofacitinib (CP-690,550). *J. Immunol.* **186**, 4234–4243
23. Menear, K. A., Adcock, C., Boulter, R., Cockcroft, X. L., Copsey, L., Cranston, A., Dillon, K. J., Drzewiecki, J., Garman, S., Gomez, S., Javaid, H., Kerrigan, F., Knights, C., Lau, A., Loh, V. M., Jr., *et al.* (2008) 4-[3-(4-cyclopropanecarbonylpiperazine-1-carbonyl)-4-fluorobenzyl]-2H-phthalazin- 1-one: A novel bioavailable inhibitor of poly(ADP-ribose) polymerase-1. *J. Med. Chem.* **51**, 6581–6591
24. Oplustil O'Connor, L., Rulten, S. L., Cranston, A. N., Odedra, R., Brown, H., Jaspers, J. E., Jones, L., Knights, C., Evers, B., Ting, A., Bradbury, R. H., Pajic, M., Rottenberg, S., Jonkers, J., Rudge, D., *et al.* (2016) The PARP inhibitor AZD2461 provides insights into the role of PARP3 inhibition for both synthetic lethality and tolerability with chemotherapy in preclinical models. *Cancer Res.* **76**, 6084–6094
25. Thorsell, A. G., Ekblad, T., Karlberg, T., Low, M., Pinto, A. F., Tresaugues, L., Moche, M., Cohen, M. S., and Schuler, H. (2017) Structural basis for potency and promiscuity in poly(ADP-ribose) polymerase (PARP) and tankyrase inhibitors. *J. Med. Chem.* **60**, 1262–1271
26. Juszczynski, P., Kutok, J. L., Li, C., Mitra, J., Aguiar, R. C., and Shipp, M. A. (2006) BAL1 and BBAP are regulated by a gamma interferon-responsive bidirectional promoter and are overexpressed in diffuse large B-cell lymphomas with a prominent inflammatory infiltrate. *Mol. Cell. Biol.* **26**, 5348–5359
27. Zhang, Y., Mao, D., Roswit, W. T., Jin, X., Patel, A. C., Patel, D. A., Agapov, E., Wang, Z., Tidwell, R. M., Atkinson, J. J., Huang, G., McCarthy, R., Yu, J., Yun, N. E., Paessler, S., *et al.* (2015) PARP9-DTX3L ubiquitin ligase targets host histone H2BJ and viral 3C protease to enhance interferon signaling and control viral infection. *Nat. Immunol.* **16**, 1215–1227
28. Fujita, T., Reis, L. F., Watanabe, N., Kimura, Y., Taniguchi, T., and Vilcek, J. (1989) Induction of the transcription factor IRF-1 and interferon-beta mRNAs by cytokines and activators of second-messenger pathways. *Proc. Natl. Acad. Sci. U. S. A.* **86**, 9936–9940
29. Haller, O., Arnheiter, H., Gresser, I., and Lindenmann, J. (1979) Genetically determined, interferon-dependent resistance to influenza virus in mice. *J. Exp. Med.* **149**, 601–612
30. Reich, N., Evans, B., Levy, D., Fahey, D., Knight, E., Jr., and Darnell, J. E., Jr. (1987) Interferon-induced transcription of a gene encoding a 15-kDa protein depends on an upstream enhancer element. *Proc. Natl. Acad. Sci. U. S. A.* **84**, 6394–6398
31. Shulman, L., and Revel, M. (1980) Interferon-dependent induction of mRNA activity for (2'-5')oligo-isoadenylate synthetase. *Nature* **288**, 98–100
32. Higashi, H., Maejima, T., Lee, L. H., Yamazaki, Y., Hottiger, M. O., Singh, S. A., and Aikawa, M. (2019) A study into the ADP-ribosylome of IFN-gamma-stimulated THP-1 human macrophage-like cells identifies ARTD8/PARP14 and ARTD9/PARP9 ADP-ribosylation. *J. Proteome Res.* **18**, 1607–1622
33. Tummino, T. A., Rezelj, V. V., Fischer, B., Fischer, A., O'Meara, M. J., Monel, B., Vallet, T., White, K. M., Zhang, Z., Alon, A., Schadt, H., O'Donnell, H. R., Lyu, J., Rosales, R., McGovern, B. L., *et al.* (2021) Drug-induced phospholipidosis confounds drug repurposing for SARS-CoV-2. *Science* **373**, 541–547
34. Blanco-Melo, D., Nilsson-Payant, B. E., Liu, W. C., Uhl, S., Hoagland, D., Moller, R., Jordan, T. X., Oishi, K., Panis, M., Sachs, D., Wang, T. T., Schwartz, R. E., Lim, J. K., Albrecht, R. A., and tenOever, B. R. (2020) Imbalanced host response to SARS-CoV-2 drives development of COVID-19. *Cell* **181**, 1036–1045.e1039
35. Iwata, H., Goettsch, C., Sharma, A., Ricchiuto, P., Goh, W. W., Halu, A., Yamada, I., Yoshida, H., Hara, T., Wei, M., Inoue, N., Fukuda, D., Mojcher, A., Mattson, P. C., Barabasi, A. L., *et al.* (2016) PARP9 and PARP14 cross-regulate macrophage activation via STAT1 ADP-ribosylation. *Nat. Commun.* **7**, 12849
36. Caprara, G., Prosperini, E., Piccolo, V., Sigismondo, G., Melacarne, A., Cuomo, A., Boothby, M., Rescigno, M., Bonaldi, T., and Natoli, G. (2018) PARP14 controls the nuclear accumulation of a subset of type I IFN-inducible proteins. *J. Immunol.* **200**, 2439–2454
37. Zschaler, J., Schlorke, D., and Arnhold, J. (2014) Differences in innate immune response between man and mouse. *Crit. Rev. Immunol.* **34**, 433–454
38. Shin, D., Mukherjee, R., Grewe, D., Bojkova, D., Baek, K., Bhattacharya, A., Schulz, L., Widera, M., Mehdipour, A. R., Tascher, G., Geurink, P. P., Wilhelm, A., van der Heden van Noort, G. J., Ovaa, H., Muller, S., *et al.* (2020) Papain-like protease regulates SARS-CoV-2 viral spread and innate immunity. *Nature* **587**, 657–662
39. Li, M., Ye, G., Si, Y., Shen, Z., Liu, Z., Shi, Y., Xiao, S., Fu, Z. F., and Peng, G. (2021) Structure of the multiple functional domains from coronavirus nonstructural protein 3. *Emerg. Microbes Infect.* **10**, 66–80
40. Michalska, K., Kim, Y., Jedrzejczak, R., Maltseva, N. I., Stols, L., Endres, M., and Joachimiak, A. (2020) Crystal structures of SARS-CoV-2 ADP-ribose phosphatase: From the apo form to ligand complexes. *IUCrJ* **7**, 814–824
41. Humphrey, W., Dalke, A., and Schulten, K. (1996) VMD: Visual molecular dynamics. *J. Mol. Graph.* **14**, 27–38
42. Jeong, J. Y., Yim, H. S., Ryu, J. Y., Lee, H. S., Lee, J. H., Seen, D. S., and Kang, S. G. (2012) One-step sequence- and ligation-independent cloning as a rapid and versatile cloning method for functional genomics studies. *Appl. Environ. Microbiol.* **78**, 5440–5443
43. Hynes, M. F., Quandt, J., O'Connell, M. P., and Puhler, A. (1989) Direct selection for curing and deletion of Rhizobium plasmids using transposons carrying the Bacillus subtilis sacB gene. *Gene* **78**, 111–120
44. Fu, Y., Sander, J. D., Reyon, D., Cascio, V. M., and Joung, J. K. (2014) Improving CRISPR-Cas nuclease specificity using truncated guide RNAs. *Nat. Biotechnol.* **32**, 279–284
45. Slaymaker, I. M., Gao, L., Zetsche, B., Scott, D. A., Yan, W. X., and Zhang, F. (2016) Rationally engineered Cas9 nucleases with improved specificity. *Science* **351**, 84–88
46. Wang, X., Spandidos, A., Wang, H., and Seed, B. (2012) PrimerBank: A PCR primer database for quantitative gene expression analysis, 2012 update. *Nucleic Acids Res.* **40**, D1144–D1149
47. Nowak, K., Rosenthal, F., Karlberg, T., Bütepage, M., Thorsell, A.-G., Dreier, B., Grossmann, J., Sobek, J., Imhof, R., Lüscher, B., Schüler, H., Plückthun, A., Leslie Pedrioli, D. M., and Hottiger, M. O. (2020) Engineering Af1521 improves ADP-ribose binding and identification of ADP-ribosylated proteins. *Nat. Commun.* **11**, 5199